JGR Space Physics

RESEARCH ARTICLE
10.1029/2020JA027890

Key Points:
- The region of sharp dipolarizations expands earthward in the inner magnetosphere while geosynchronous dipolarizations are sustained
- Dipolarizations at r < 5 R_e are often smooth and gradual resembling midlatitude positive bays, and start simultaneously with substorm onsets
- In the inner magnetosphere, sharp dipolarizations start earlier off the equator, often before geosynchronous dipolarizations

Supporting Information:
- Supporting Information S1

Correspondence to:
S. Ohtani,
ohtani@jhuapl.edu

Citation:
Ohtani, S., Motoba, T., Takahashi, K., & Califf, S. (2020). Generalized substorm current wedge model: Two types of dipolarizations in the inner magnetosphere. *Journal of Geophysical Research: Space Physics*, *125*, e2020JA027890. https://doi.org/10.1029/2020JA027890

Received 6 FEB 2020
Accepted 11 AUG 2020
Accepted article online 22 AUG 2020

Generalized Substorm Current Wedge Model: Two Types of Dipolarizations in the Inner Magnetosphere

S. Ohtani[1], T. Motoba[1], K. Takahashi[1], and S. Califf[2]

[1]The Johns Hopkins University Applied Physics Laboratory, Laurel, MD, USA, [2]Cooperative Institute for Research in Environmental Sciences, University of Colorado Boulder, Boulder, CO, USA

Abstract The present study investigates dipolarization signatures in the inner magnetosphere using sharp geosynchronous dipolarizations as a reference. The results are summarized as follows: (1) The region of sharp and structured dipolarizations expands earthward while dipolarizations are sustained at geosynchronous orbit; (2) within 5 R_E from Earth, dipolarization signatures are often smooth and gradual, resembling midlatitude positive bays, and they start simultaneously with substorm onsets; (3) off the equator (>0.5 R_E), sharp dipolarizations often take place before geosynchronous dipolarizations. These results can be explained by a model current system with R1-sense and R2-sense current wedges (R1CW and R2CW) if (a) the R1CW, which is located outside, is more intense than the R2CW in total current, (b) the R1CW stays outside of geosynchronous orbit, and (c) the R2CW moves earthward. The model suggests that the region of sharp dipolarizations is confined between the two current wedges, and it expands earthward as the R2CW moves earthward (Result 1). Sufficiently earthward of the R2CW, the remote effect of the R1CW dominates that of the R2CW, and accordingly, magnetic disturbances resemble midlatitude positive bays (Result 2). Since the timing of sharp dipolarizations is determined by the passage of the R2CW, they take place earlier for outer flux tubes. Away from the magnetic equator, sharp dipolarizations can precede geosynchronous dipolarizations especially if the magnetic configuration is stretched (Result 3). Thus, this double-current wedge model explains the variability of dipolarization signatures at different distances, and it may be regarded as a generalized substorm current wedge model.

1. Introduction

The substorm current wedge (SCW) model proposes that at the onsets of substorms the cross-tail current partially short-circuits to the high-latitude ionosphere through a pair of downward and upward (i.e., into and out of the ionosphere) field-aligned currents (FACs) at the dawnside and duskside edges, respectively (McPherron et al., 1973). Despite its simplicity, the model explains the basic characteristics of not only geosynchronous dipolarizations but also midlatitude positive bays on the ground (Clauer & McPherron, 1974).

Nevertheless, the SCW has one difficulty in explaining dipolarizations in the inner magnetosphere, which may have been largely overlooked but probably deserves closer attention. According to the SCW model, dipolarizations take place simultaneously anywhere inside the current wedge; more accurately, it is expected to take place within the Alfvén travel time along the magnetic field line between the magnetosphere and ionosphere. However, Ohtani et al. (2018) (hereafter referred to as O2018) reported that inside geosynchronous orbit the occurrence probability of dipolarizations (as defined as sharp increases in the northward magnetic component) decreases sharply toward Earth, and the region of dipolarizations expands earthward at a finite velocity, ~50 km/s, much slower than the Alfvén velocity. These results apparently contradict the conventional SCW model.

O2018 explained these results in terms of two wedge currents, one with the R1 sense and another with the R2 sense. The R1-sense current wedge (R1CW) is the primary component as expected from the conventional SCW model, and the R2-sense current wedge (R2CW) is secondary and is located earthward of the R1CW. Earthward of the R2CW, the magnetic effects of those two current wedges partially cancel each other. Accordingly, dipolarizations are confined between these two current wedges, and its region expands earthward as the R2CW proceeds earthward, which may result from the change of plasma pressure due to particle injection.

Double-current wedge systems have been considered for two fundamental processes of magnetotail dynamics, that is, dipolarization fronts and flow braking; see a review article by Kepko et al. (2015). The radially confined enhancement of the equatorial magnetic field is a characteristic feature of dipolarization fronts, for which a double-wedge current system was deduced by synthesizing satellite magnetic field observations (Liu et al., 2013). For the braking of fast plasma-sheet flows, which is generally explained in terms of the interchange motion of depleted flux tubes (Wolf et al., 2009), the formation of a double-current wedge system was simulated by a regional MHD model (e.g., Birn et al., 1999) and the Rice Convection Model (Yang et al., 2012), and has been discussed in the context of the SCW formation at substorm onsets. Possibly related to the flow braking, a tail configuration with radially confined dipolarizations outside geosynchronous orbit was reported for a quiet-time substorm(-like) event and quantitatively explained with a double-wedge current model (Sergeev et al., 2014).

It still remains to be understood how, or if, dipolarizations in the inner magnetosphere are related to those two magnetotail processes. Such dipolarizations may be a manifestation of the deep penetration of depleted flux tubes into the inner magnetosphere (e.g., Gkioulidou et al., 2015). The idea is appealing especially because the dipolarization region expands earthward, and the associated R2CW may be the one intrinsic to the dipolarization fronts. However, if this is the case, we need to understand why dipolarizations are often sustained at geosynchronous orbit. On the other hand, dipolarizations in the near-Earth region are one of the characteristic features of substorms, and therefore, the associated R2CW may be the one predicted by the flow braking model. However, if this is the case, it is not clear how the dipolarization region expands earthward. In addition to these two possibilities, local plasma instabilities may contribute to the formation and development of the SCW. Obviously understanding the responsible process of dipolarizations in the inner magnetosphere is a challenge, which requires extensive observational and modeling studies. In the present study, we examine dipolarizations in the inner magnetosphere focusing on their spatial structure and development, and seek to place observational constraints on modeling the associated current system.

The present study is complementary to O2018's study in three ways. First, in this study, we examine a substorm event in detail with multi-satellite and ground data; in contrast, O2018's study was statistical. Second, we adopt geosynchronous dipolarizations as a reference and then examine magnetic disturbances in the inner magnetosphere. Although geosynchronous altitude is not special in itself for substorm dynamics, the association of geosynchronous dipolarizations with substorms was well established by numerous studies (e.g., Liou et al., 2002), and they help understanding dipolarizations in the inner magnetosphere in terms of substorm dynamics. O2018, in contrast, used as a reference sharp dipolarizations observed in the inner magnetosphere. Third, we address the spatial development of dipolarizations in the meridional plane, rather than in the equatorial plane (as O2018 did). Through these research tasks, we seek to verify and refine the aforementioned two-wedge current model.

The rest of this paper is organized as follows. In section 2, we briefly describe satellite magnetometer data we use in this study. In section 3, we examine a dipolarization event of 31 March 2017, in which multiple satellites were distributed fortuitously in the near-Earth region. In section 4, we statistically examine magnetic signatures observed inside geosynchronous orbit referring to sharp geosynchronous dipolarizations observed in the same sector. We discuss the results in section 5 and summarize the study in section 6.

2. Satellite Data

For examining dipolarizations in the inner magnetosphere we use data obtained from the Van Allen Probes (RBSP) mission (Mauk et al., 2012). The RBSP mission consists of two identical spacecraft (Probes A and B), which were launched in August 2012 into an equatorial orbit with an orbital inclination of 10°, an apogee distance of 5.8 R_E, and an orbital period of ~9 hr. In this study we use 1-s averages of magnetic field measurements made by the Electric and Magnetic Field Instrument Suite and Integrated Science (EMFISIS) experiment (Kletzing et al., 2013) from September 2012 to December 2017.

For examining geosynchronous dipolarizations we use magnetic field data obtained from the GOES-13 (G13), GOES-14 (G14), and GOES-15 (G15) geosynchronous satellites. The G13 and G15 data are available for the entire period of the RBSP data set, whereas the G14 data are available for intermittent periods with a total duration of about a year. The geographic longitude (GLon) and magnetic latitude (MLat) of their locations were (75°W, 9°) for G13, (105°W, 8°) for G14, and (135°W, 4–5°) for G15. The time resolution of the

Table 1

Locations of Satellites and Ground Stations at 0420 UT on 31 March 2017

	MLT	MLat	r (R_E)
RBSP-A	20.5	−2.7°	4.9
RBSP-B	21.3	−1.5°	3.5
GOES-13	23.2	9.3°	6.6
GOES-14	21.3	8.3°	6.6
GOES-15	19.2	4.4°	6.6
THEMIS-A	20.3	0.3°	13.3
THEMIS-D	20.2	4.3°	11.1
THEMIS-E	20.6	3.8°	11.8
Gillam (GILL)	21.7	66.2°	1.0
Fresno (FRN)	19.8	42.7°	1.0
Boulder (BOU)	20.9	48.5°	1.0
Fredericksburg (FRD)	23.5	48.1°	1.0

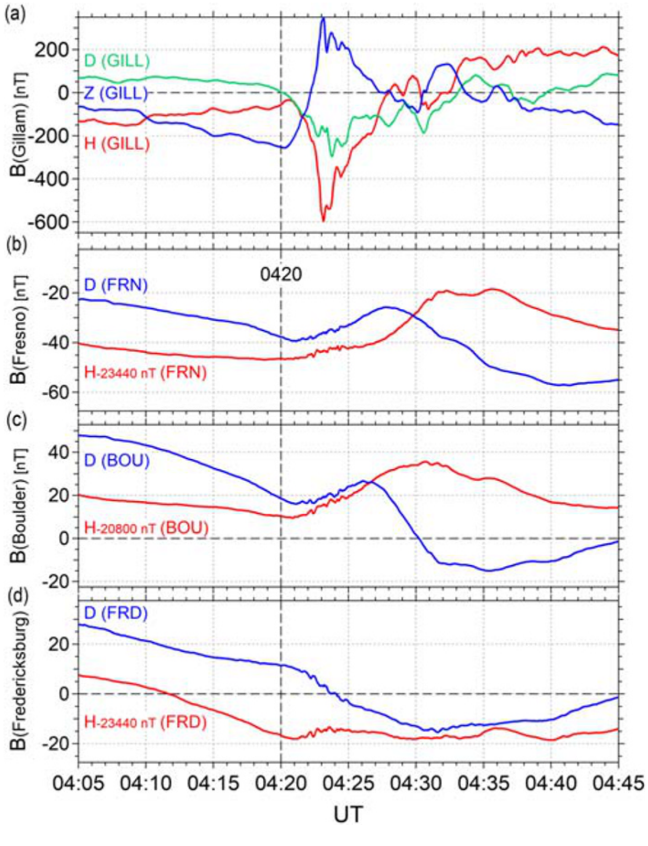

Figure 1. (a) Northward (H; red), eastward (D; blue), and vertically downward (Z; green) magnetic components observed at GILL, and the H (red) and D (blue) components observed at (b) Fresno (FRN), (c) Boulder (BOU), and (d) Fredericksburg (FRD) on 31 March 2017. The GILL data are provided in the SuperMAG *NEZ* coordinate system (Gjerloev, 2012), and N, E, and Z are considered, for any practical purpose, as the disturbance parts of the H, D, and Z components, respectively, and therefore, are presented as such. For FRN, BOU, and FRD, the H component has offset as annotated in each panel, and the D component is converted from the magnetic deflection to nT.

original data is 0.512 s for each GOES satellite, and we resample the data at 1-s cadence for examining the correlation with RBSP signatures. We also use 10-s averages for preliminarily selecting events for the statistical study (section 4).

For our event study (section 3), we also use 3-s spin averages of magnetic field measurements (Auster et al., 2008) made by the three THEMIS satellites, THEMIS-A (THA), THEMIS-D (THD), and THEMIS-E (THE) (Angelopoulos, 2008), which were located outside of 11 R_E in the event.

For the RBSP and GOES magnetometer data we use the *VDH* cylindrical coordinate system. The H axis is anti-parallel to the terrestrial magnetic dipole, positive northward. The V axis is in a plane that includes the H axis and the radial vector from the center of Earth to the satellite location, and it is perpendicular to the H axis and is positive outward. The D axis completes a right-hand orthogonal system and is positive eastward. For the THEMIS magnetometer data, we use the Geocentric Solar Magnetospheric (GSM) coordinate system. Whereas the *VDH* system is appropriate for the near-Earth region, where the terrestrial dipole field makes a major contribution to the magnetic configuration, the GSM system is more appropriate for the magnetotail, where the contribution of the tail current is dominant.

3. 31 March 2017 Event

In this section we examine a dipolarization event that was observed on 31 March 2017. The event took place in the middle of the prolonged recovery phase of a storm. Since the *Sym-H* index reached its minimum at −86 nT more than 3 days before, substorm activity had been continuously high corresponding to highly varying interplanetary magnetic fields.

All-sky image data at Gillam (GILL) show that the initial auroral brightening took place at 0420 UT to the south of the station (not shown), which we identify as the onset of this substorm event; GILL was at 21.8 in magnetic local time (MLT) and 66.2° in geomagnetic latitude (MLat) in the Altitude Adjusted Corrected Geomagnetic (AACGM) coordinates (see Table 1). Figure 1a shows the three magnetic field components observed GILL. The northward (H; red) magnetic component started to decrease sharply at 0421 UT, whereas the vertically downward (Z) component started to increase at 0420 UT, simultaneously with the substorm onset, indicating that the westward auroral electrojet initially intensified to the south of GILL. H decreased by ~600 nT within a few minutes. Subsequently, auroral intensification extended over the entire North American sector, and a westward traveling surge was observed at Fort Simpson (MLT = 19.2 and MLat = 67.5°) at 0427 UT (not shown). Whereas the spatial extension of this substorm was typical, the duration of its expansion phase was short, and all geomagnetic and auroral activity decayed within 10 min (not shown).

Figures 1b–1d show the H (red) and D (blue: eastward) magnetic components observed at three midlatitude stations, Fresno (FRN), Boulder (BOU), and Fredericksburg (FRD), from the west to the east; see Table 1 for their locations. At 0421 UT, H started to increase at

UT	Ground	RBSP (RBSP-A & RBSP-B)	GOES (G13,G14 & G15)	THEMIS (THA,THD & THE)
04:19				• Sustained Bz increase (THD,THE)
04:20	• Auroral Brightening (GILL) • Z increase (GILL) • H decrease (GILL)	• Smooth ΔH increase (RBSP-B)	• Transient ΔH increase (G14) • Increases in |ΔV| and ΔD (G14)	
04:21	• Positive Bay Onset (FRN, BOU & FRD)			
04:22		• Smooth ΔH increase (RBSP-A; likely earlier)	• ΔH dip & sustained increase (G15) • Sustained ΔV recovery & transient ΔH increase (G13)	
04:23	• H ~-600 nT (GILL)		• Sustained ΔH increase (G14) • Positive ΔD peak (G15)	
04:24			• Negative ΔD peak (G13)	
04:25		• ΔH dip & sustained increase (RBSP-A)		
04:26				
04:27	• Westward Traveling Surge (Fort Simpson)			

Figure 2. Sequence of the start times (unless specified) of substorm features observed on the ground and in space.

each station, which can be identified as a midlatitude positive bay. The 1-min delay of its onset from the substorm onset might be attributed to the initial localization of the SCW around the GILL meridian. D increased at FRN and BOU, whereas it decreased at FRD, suggesting that the substorm current system was centered between BOU and FRD in longitude and extended 3–4 hr in MLT (Clauer & McPherron, 1974). At each station both H and D fluctuated for several minutes after the onset. These fluctuations are Pi2 pulsations, a well-known identifier of substorm onsets. The sequence of those ground features is shown in Figure 2 along with magnetospheric substorm signatures, which we examine next.

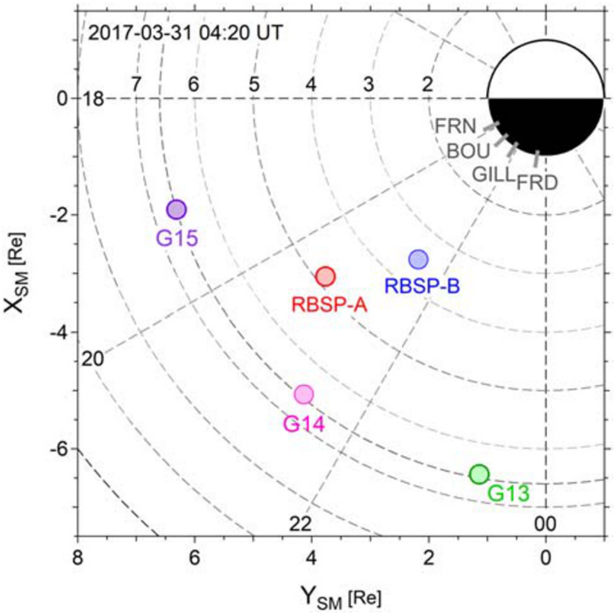

Figure 3. The locations of RBSP-A (red), RBSP-B (blue), G13 (green), G14 (magenta), and G15 (purple) in the X-Y plane of the SM coordinate system at 0420 UT on 31 March 2017 along with the longitudes of Fresno (FRN), Boulder (BOU), Gillam (GILL), and Fredericksburg (FRD) as marked by the gray short segments at Earth.

Figure 3 shows the locations of the two RBSP satellites, RBSP-A and RBSP-B, and three GOES satellites, G13, G14, and G15, in the X-Y plane of the Solar Magnetic (SM) coordinate system at 0420 UT. The MLT, MLat, and radial distance (r) of each satellite are also listed in Table 1. RBSP-A was located at $r = 4.9\ R_E$ between G15 and G14 in MLT. RBSP-B was located closer to Earth, at $r = 3.7\ R_E$, almost at the same meridian as G14. Whereas all three GOES satellites were located in the northern hemisphere, the two RBSP probes were located slightly below the magnetic equator. The short gray segments at Earth mark the meridians of the aforementioned ground stations, from which we infer that the sector of the initial formation of the substorm current system was well covered by those five satellites.

Figure 4 shows, from the top, the V, H, and D magnetic components observed by RBSP-A (red), RBSP-B (blue), G15 (purple), G14 (magenta), and G13 (green) during the interval 0405–0445 UT. We put aside RBSP-B for now and quickly look over magnetic signatures observed by the other four spacecraft. The H component at RBSP-A was larger than that at geosynchronous orbit (Figure 4b) because of its location closer to Earth, and it increased with time as RBSP-A was on an inbound pass. All four satellites observed an increase in the H component, dipolarization, along with large fluctuations at 0420–0430 UT. The dipolarization was observed first at geosynchronous orbit and then at RBSP-A. The V component was positive at

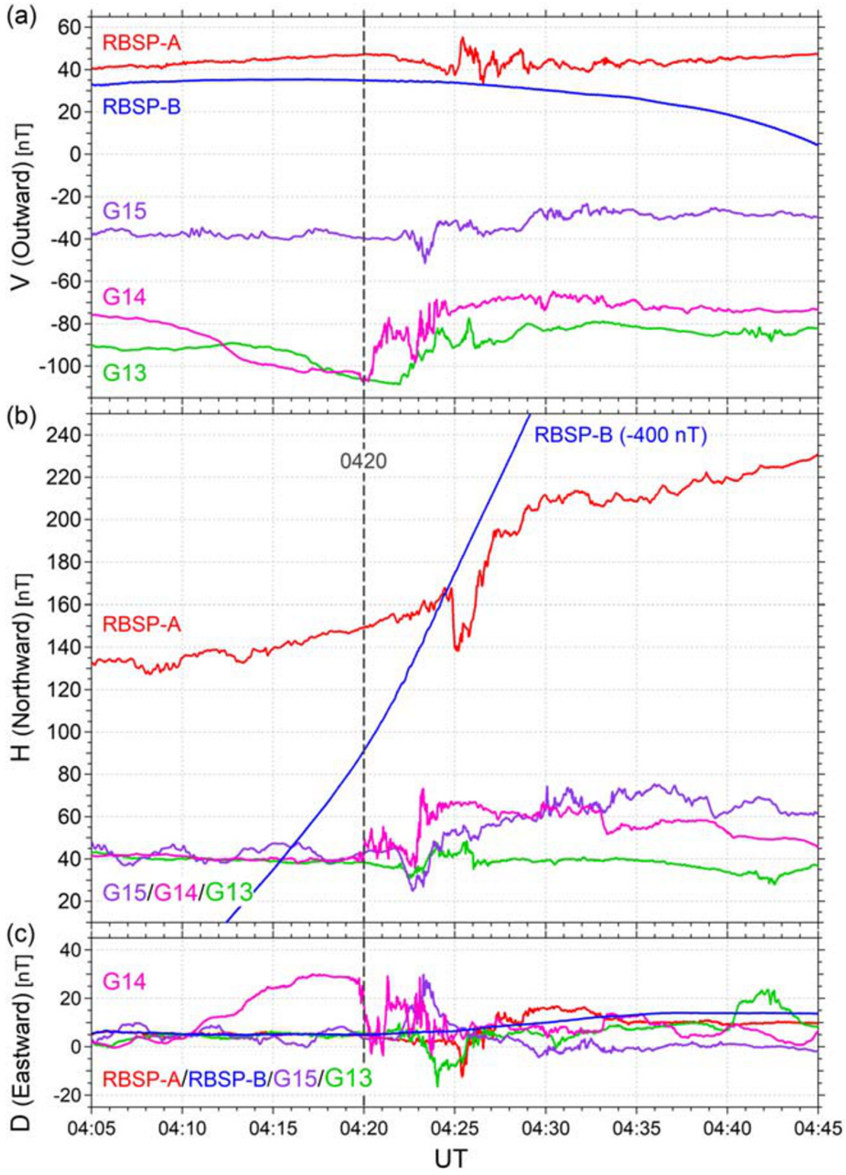

Figure 4. (a) *V*, (b) *H*, and (c) *D* magnetic components observed by RBSP-A (red), RBSP-B (blue), G15 (purple), G14 (magenta), and G13 (green) on 31 March 2017. The RBSP-B *H* component is offset by −400 nT.

RBSP-A, whereas it was negative at each GOES satellite (Figure 4a), reflecting their locations relative to the magnetic equator (Table 1). At G14 and G13 the *V* component gradually decreased (its magnitude increased) before the substorm onset, which can be attributed to the intensification of the local westward current. Such an increase in $|V|$ was unclear at RBSP-A and G15 presumably because those satellites were closer to the magnetic equator. The *D* component also changed positively and negatively in association with the dipolarization (Figure 4c).

Now we examine dipolarization-related magnetic variations observed by the RBSP and GOES satellites one by one. In the rest of this study we examine the difference between the measured magnetic field and the quiet-time ($Kp = 0$) T89 model field (Tsyganenko, 1989), which removes most of the change of the background magnetic field associated with the satellite motion and allows focusing on substorm-related disturbances especially for the RBSP probes.

Figure 5 shows, from the top, the *V*-, *H*-, and *D*-component differences (ΔV, ΔH, and ΔD) at G13 (green), G14 (magenta), and G15 (purple) during the interval 0410–0435 UT. We start with G14. A transient increase in

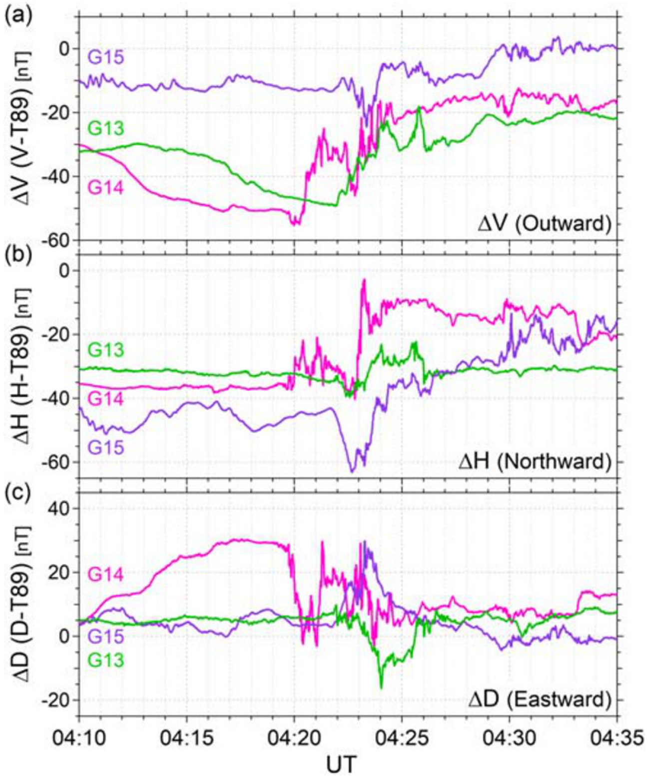

Figure 5. (a) ΔV, (b) ΔH, and (c) ΔD at G13 (green), G14 (magenta), and G15 (purple) on 31 March 2017.

ΔH started at 0420 UT, which was followed by a larger and sustained increase starting at 0423 UT (Figure 5b). The magnitude of ΔV, $|\Delta V|$, and ΔD tended to increase before 0420 UT, and then they started to decrease (Figures 5a and 5c). These increase and decrease (in $|\Delta V|$ and ΔD) correspond to the stretching and relaxation of the local magnetic configuration, respectively. This relaxation was sustained, and it can be attributed to the reduction of the local tail current (or the ring current). Its start coincided with the ground substorm onset, suggesting that G14 was located close to the onset meridian as we addressed earlier (see Figures 1 and 3).

Now let us move on to G15 and G13, which were located to the west and east of G14, respectively (Figure 3). At G15 ΔH started to increase at 0422:40 UT following a sharp ~20-nT reduction and followed by a sustained enhancement (Figure 5b). At G13 ΔH also increased around the same time, but the enhancement was transient and smaller in magnitude. On the other hand, ΔV at G13 revealed a sustained recovery starting at 0422 UT (Figure 5a). Although the exact timing of local dipolarization onsets may be difficult to identify for G15 and G13, they obviously delayed from the 0420 UT dipolarization onset at G14.

At G15 and G13 ΔD changed positively (eastward) and negatively (westward), respectively, around the onsets of local dipolarizations (Figure 5c). If these ΔD variations were caused by FACs poleward of the spacecraft, they flowed out of the ionosphere at G15 and to the ionosphere at G13, and therefore, the FACs had the R1-sense polarity. The SCW model suggests that the substorm current system, which formed around the G14 meridian, expanded westward and eastward over the next 3–4 min reaching the G15 and G13 meridians.

Figure 6 shows ΔV, ΔH, and ΔD at RBSP-A (red) and RBSP-B (blue) along with those at G14 (dotted magenta) and the ground H component at Boulder (black; see also Figure 1); for RBSP-B, 11-s sliding averages are used to remove spin modulations. At RBSP-A, ΔH started to increase at 0425 UT immediately following a large sharp reduction. By that time dipolarizations already started at G14 and G15, which were located to the east and west of RBSP-A, respectively. Therefore, this RBSP-A observation strongly suggests that the region of sharp dipolarizations expanded earthward. The expansion velocity is estimated at 36 km/s by dividing the radial separation between RBSP-A and G14, 1.7 R_E, by the corresponding time delay (0425 UT at RBSP-A vs. 0420 UT at G14), or at 60 km/s if we use the time delay from the G15 onset instead. The estimates are consistent with the statistical result of O2018.

The radial profile of the azimuthal electric current can be inferred from the temporal variation of ΔH observed by RBSP-A assuming that it actually represents a radial structure that passed the satellite as it moved earthward. The sharp ΔH reduction at the start of the ΔH dip represents a radially localized eastward current, and the subsequent increase represents a more extended westward current. At the estimated velocity of the earthward expansion of the dipolarization region, 36 km/s, the radial extents of the eastward and westward currents are estimated at 400 km and 0.7 R_E, respectively. (Whereas the former is of the order of the thermal (tens of keV) ion gyroradius, the latter is larger by an order of magnitude; in contrast, for dipolarization fronts, both are comparable to the local thermal ion gyroradius (Runov et al., 2011).) Presumably these eastward and westward currents partially closed with each other in the magnetosphere. This is consistent with the idea that the ΔH reduction is a diamagnetic signature collocated with a plasma pressure enhancement, and the loop of the associated diamagnetic current confines the ΔH reduction in a narrow range of the radial distance (e.g., Yang et al., 2011).

Most importantly, the ΔH reduction was smaller in magnitude than the subsequent increase in a ratio of 1:2, and therefore, the total westward current exceeded the total eastward current. If this excess westward current closed, at least partially, through the ionosphere, the associated FAC system had the R2-sense

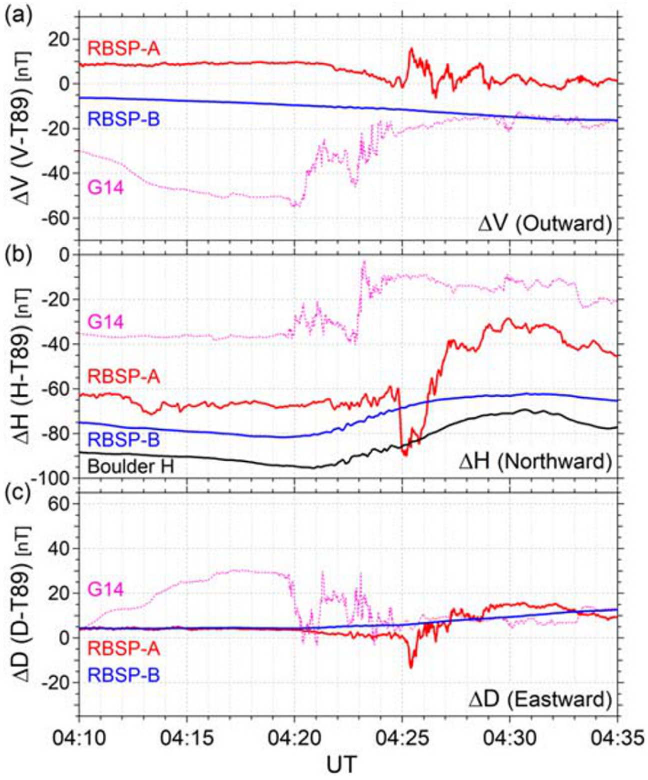

Figure 6. (a) V, (b) H, and (c) D magnetic components observed by RBSP-A (red) and RBSP-B (blue) as well as G14 (dotted magenta) on 31 March 2017. Also plotted in Figure 6b is the H ground magnetic component at Boulder with an arbitrary offset (black).

polarity. We will discuss later that the co-existence of the R2CW (with the R1CW) is essential for the radial confinement and earthward expansion of the dipolarization region.

At RBSP-B, a prolonged hump of ΔH started around 0420 UT simultaneously with the local dipolarization at G14 and 5 min earlier than the onset of the local dipolarization at RBSP-A, even though RBSP-B was located closer to Earth than RBSP-A. Moreover, ΔH at RBSP-B changed in parallel with the midlatitude positive bay at Boulder; note that both RBSP-B and Boulder were located in the sector of the initial SCW formation (see also Figures 1 and 3). Midlatitude positive bays are generally considered as a remote effect of the SCW system (Clauer & McPherron, 1974), and the similarity between the RBPS-B ΔH and Boulder H signatures suggests that this is also the case for the ΔH increase at RBSP-B. RBSP-B did not observe any clear enhancement of energetic ion and electron fluxes (not shown), which supports the idea that this ΔH increase at RBSP-B was a remote effect. We also note that RBSP-B observed a Pi2 pulsation.

Interestingly, a hint of this gradual dipolarization can be found in the RBSP-A signature. At RBSP-A ΔH started to increase at 0422 UT at latest, and similar gradual changes in ΔV and ΔD started slightly earlier. These variations may also be the remote effect of the same current system that caused a gradual dipolarization at RBSP-B. In contrast, RBSP-B did not observe any signature that can be associated with the ΔH dip observed by RBSP-A around 0425 UT, which suggests that the ΔH dip was localized around RBSP-A as we addressed earlier.

Finally, we briefly examine magnetic signatures observed by the three THEMIS probes, which were located in the same sector but outside of 11 R_E (Figure 7a). Figures 7b–7d show B_X (dashed), B_Y (dotted), and B_Z (solid) magnetic components in GSM coordinates observed by THA, THD, and THE, respectively. For each satellite B_Z was much smaller in magnitude than the other components for most of the interval, suggesting that those probes were away from the neutral sheet, and it is not straightforward to identify the local onsets of substorm-related disturbances, especially for THA. Nevertheless, at THD and THE, B_Z started to increase around 0419 UT, 1 min before the dipolarization onset at G14. If this time delay was caused solely by the earthward expansion of the dipolarization region, its velocity is estimated at ~400 km/s, which suggests that the observed B_Z enhancements at THD and THE were associated with a fast plasma flow; the direct measurement of the convection flow is not available as the satellites were off the neutral sheet. We also note that those B_Z enhancements were sustained rather than transient, and therefore, it is possible that the R1CW already formed outside of the THEMIS distance when B_Z started to increase at THD and THE. In either way the THEMIS observation suggests that the change of the magnetic configuration started outside of geosynchronous orbit.

4. Statistical Study

In the 31 March 2017 event (section 3) the RBSP probes observed two completely different types of dipolarizations in the inner magnetosphere. RBSP-A observed a sharp and structured dipolarization, for which we found that the dipolarization region expanded earthward while the geosynchronous dipolarization was sustained. In contrast, closer to Earth, RBSP-B observed a gradual dipolarization, which appeared to start simultaneously with the formation of the SCW. This latter kind of dipolarizations would be easily overlooked unless we use geosynchronous dipolarizations as a time reference and subtract the background magnetic field; see Figure 4b for the original H component observed by RBSP-B. Guided by this result, in this section we statistically examine dipolarization signatures in the inner magnetosphere using sharp geosynchronous dipolarizations as a reference.

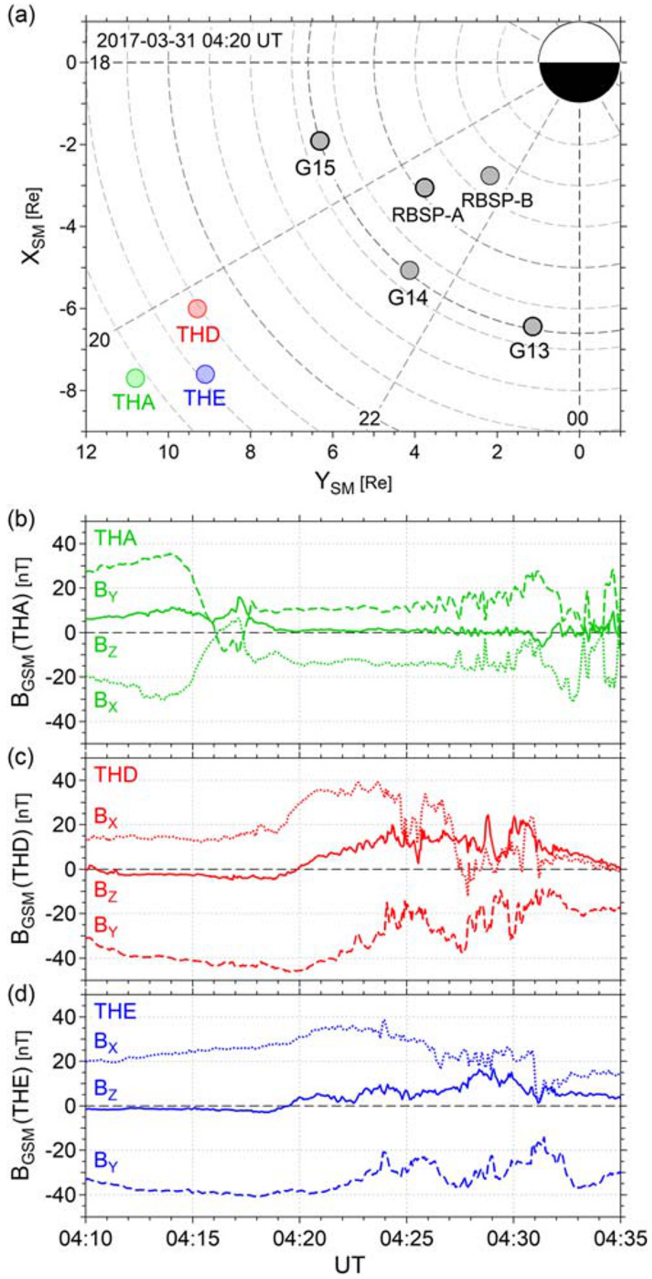

Figure 7. (a) Equatorial locations of THA (green), THD (red), and THE (blue) probes along with those of RBSP-A, RBSP-A, G13, G14, and G15 (all gray) at 0420 UT on 31 March 2017; B_X (dotted), B_Y (dashed), and B_Z (solid) magnetic components observed by (b) THA, (c) THD, and (d) THE on 31 March 2017.

For selecting GOES dipolarization events we used 10-s averages of ΔH (section 2). We selected events in which ΔH increased by more than 10 nT within 90 s ($\Delta H_{\max} - \Delta H_{\min} > 10$ nT; $\Delta H_{\max}$ and $\Delta H_{\min}$ are the maximum and minimum of ΔH during the 90-s interval), and the increase was step-like; ΔH stayed above $(\Delta H_{\max} + \Delta H_{\min})/2$ for at least 5 min after $\Delta H_{\max}$. We did not impose a similar requirement to the interval before $\Delta H_{\min}$ since sharp dipolarizations are often preceded by a dip of ΔH (Ohtani et al., 1992) as we saw in section 3. In addition, the selected events cannot be preceded by any other such ΔH increase within 15 min before.

For events in which at least one RBSP probe was at $r \geq 4\ R_E$ and within 0.5 hr in MLT from the GOES meridian, we examined the correlation of ΔH variations at GOES and RBSP spacecraft using 1-s data. We took as a reference the GOES ΔH variations during the 10 min interval centered at the start of the ΔH increase and sought for the maximum correlation by shifting a 10-min time window of the RBSP data from -5 to $+5$ min every second. We additionally examined the correlation of the linearly detrended variations of ΔH in the same way.

For adopting the time delay of ΔH signatures as that of dipolarization signatures, we required that (i) the correlation coefficient (c.c.) of ΔH exceed 0.6, (ii) the GOES-RBSP amplitude ratio of ΔH be between 0.5 and 2, (iii) the c.c. of detrended ΔH exceed 0.5, and (iv) the time difference of ΔH variations agree with that of detrended ΔH variations within 15 s. We adopted (ii)–(iv) to avoid misidentifying monotonous increases in ΔH as dipolarizations, which very often took place as RBSP moved radially (even if we subtracted the quiet-time model magnetic field). Note that the correlation of ΔH is not a sufficient measure for excluding monotonous increases; for example, the c.c. between a linear increase and a step jump is as high as 0.86. Finally, for each selected event, we visually examined the plots of all three magnetic components of each satellite as well as the dependence of the c.c. on the time shift (see Figure 4 of O2018). In total, we selected 22 events. In addition, we found 14 events, in which ΔH increased smoothly and gradually as observed by RBSP-B in the 31 March 2017 event. We refer to such events as positive bay-like dipolarizations. They did not meet at least one of the aforementioned four conditions, (i)–(iv). The event list of each type of dipolarizations is available in the supporting information.

Figure 8 shows the locations of the RBSP spacecraft in Z versus r_{xy} in SM coordinates for the 22 selected events (circles) and 14 positive bay-like events (green hexagons); r_{xy} is the equatorial distance of the satellite from the center of Earth. The size of the circles indicates the c.c., whereas its color indicates the time difference, ΔT. If the color is bluish ($\Delta T < 0$) and reddish ($\Delta T > 0$), the RBSP signature was ahead and behind of the GOES signature in time, respectively.

There are two points to make. First, ΔT is mostly positive near the equator, whereas away from the equator, it is clearly more negative than positive. That is, dipolarizations tend to take place earlier for outer flux tubes. Figure 9 shows the pre-dipolarization magnetic inclination, $\tan^{-1}(H/|V|)$, at RBSP against that of the T89 model field for each event. It is clear that the magnetic field before dipolarizations is generally far more stretched than the T89 model, suggesting that in the off-equator events, the RBSP field line was possibly located outside of the GOES field line. It is therefore inferred from Figure 8 that the timing of

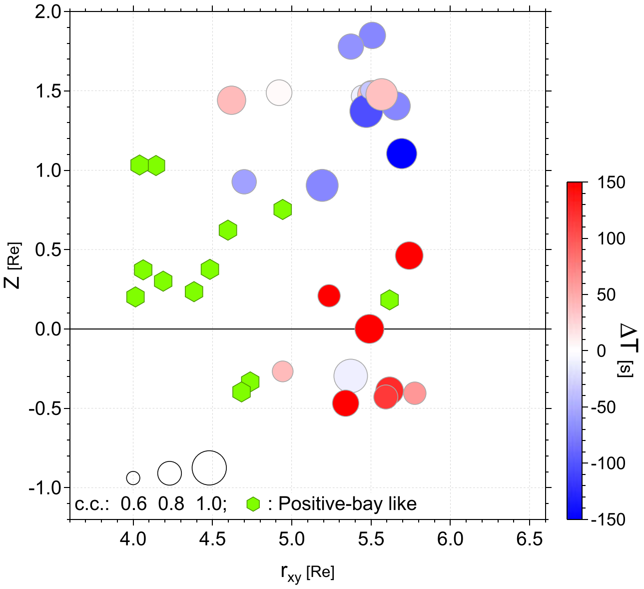

Figure 8. Locations of the RBSP spacecraft for GOES dipolarization events in the meridional (r_{xy}-Z) plane. The size of the circles indicates the correlation coefficient of ΔH variations at RBSP and GOES (see the reference circles at the bottom left), whereas the color indicates the time delay of RBSP signatures from GOES signatures as indicated by the color bar. The green hexagons represent positive bay-like dipolarizations at RBSP. See text for details.

dipolarizations is better organized by the equatorial distance of the satellite field line than by the satellite radial distance. The present result may be considered as a generalization of the previously reported result that dipolarizations propagate earthward in the equatorial plane (Ohtani, 1998; O2018; Russell & McPherron, 1973).

Second, positive bay-like dipolarizations were distributed mostly earthward of the structured dipolarizations. For those events we found that the ΔH enhancements at RBSP started around the time when the geosynchronous magnetic configuration started to change at GOES; for some events, however, the ΔH increase at RBSP was so gradual that its onset was difficult to specify. It is suggested that the positive bay-like dipolarizations reflect the global, as opposed to local, development of the substorm current system as we found for the 31 March 2017 event (section 3).

In closing, we quickly examine two examples of positive bay-like dipolarizations; for sharp dipolarizations propagating earthward, additional examples may be found in O2018. In the first example (Figure 10a), which took place on 2 March 2013, G13 (blue) observed at MLT = 22.8 that ΔH started to increase around 0400 UT, whereas ΔV and ΔD started to change a few minutes earlier simultaneously with a slight ΔH decrease. The large (>30 nT) positive ΔD excursion suggests that G13 was around the western edge of the SCW system. In contrast, at RBSP-A (red), which was located $r_{xy} = 4.4\ R_E$ slightly closer to midnight (MLT = 23.1), ΔV and ΔD did not change significantly, but ΔH started to increase around the time when ΔV and ΔD started to change at G13. At the same time, a midlatitude positive bay started at Boulder along with a Pi2 pulsation (black line in the ΔH panel), suggesting that the SCW formed at the start of the gradual ΔH increase at RBSP-A.

The second event took place on 22 August 2013, which is shown in Figure 10b. G15 (blue) was located in the late evening sector (MLT = 21.4 at 0630 UT), and RBSP-B (red) was located slightly duskward (MLT = 20.9) at $r_{xy} = 4.5\ R_E$. ΔH at G15 increased sharply at 0630:30 UT, followed by another sharp increase ~15 min later. Each ΔH increase was accompanied by the reduction of $|\Delta V|$ and positive excursion of ΔD. At RBSP-B, ΔH was initially flat, but around the time of the first ΔH increase at G15, it increased by a few nT and continued to increase but more gradually. Then, at 0643 UT, ΔH made another noticeable increase in the slope, which took place a few minutes before the second ΔH increase at G15 but simultaneously with the start of the ΔV and ΔD changes at G15. Each ΔH increase at RBSP-B started simultaneously with a midlatitude H increase at Fresno (black line in the ΔH panel). Here again it is suggested that these positive bay-like dipolarizations were manifestations of the formation of the SCW.

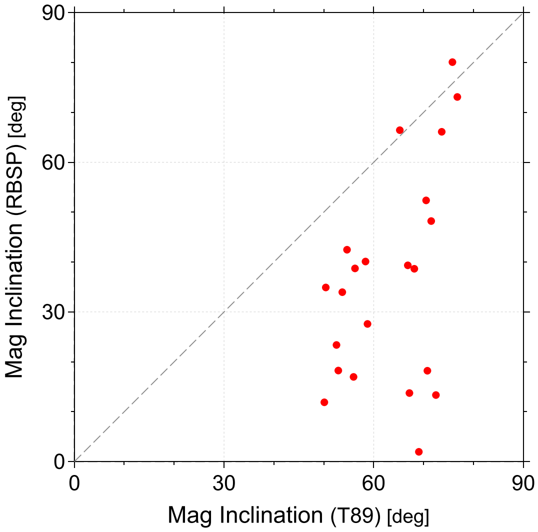

Figure 9. Magnetic inclinations, $\tan^{-1}(H/|V|)$, at RBSP at the onset of GOES dipolarizations against those of the T89 ($Kp = 0$) model field for the sharp and structured RBSP dipolarizations.

5. Discussion

In the present study we examined the 31 March 2017 event with multi-satellite data (section 3) and also statistically examined the timing and characteristics of RBSP dipolarizations using sharp geosynchronous dipolarizations as a reference (section 4). We confirmed that (1) the region of sharp dipolarizations expands earthward while geosynchronous dipolarizations are sustained. In the 31 March 2017 event the earthward expansion started outside of geosynchronous orbit and slowed down as it approached Earth. We additionally found that (2) further close to Earth, mostly within 5 R_E, positive bay-like dipolarizations start simultaneously with global magnetic

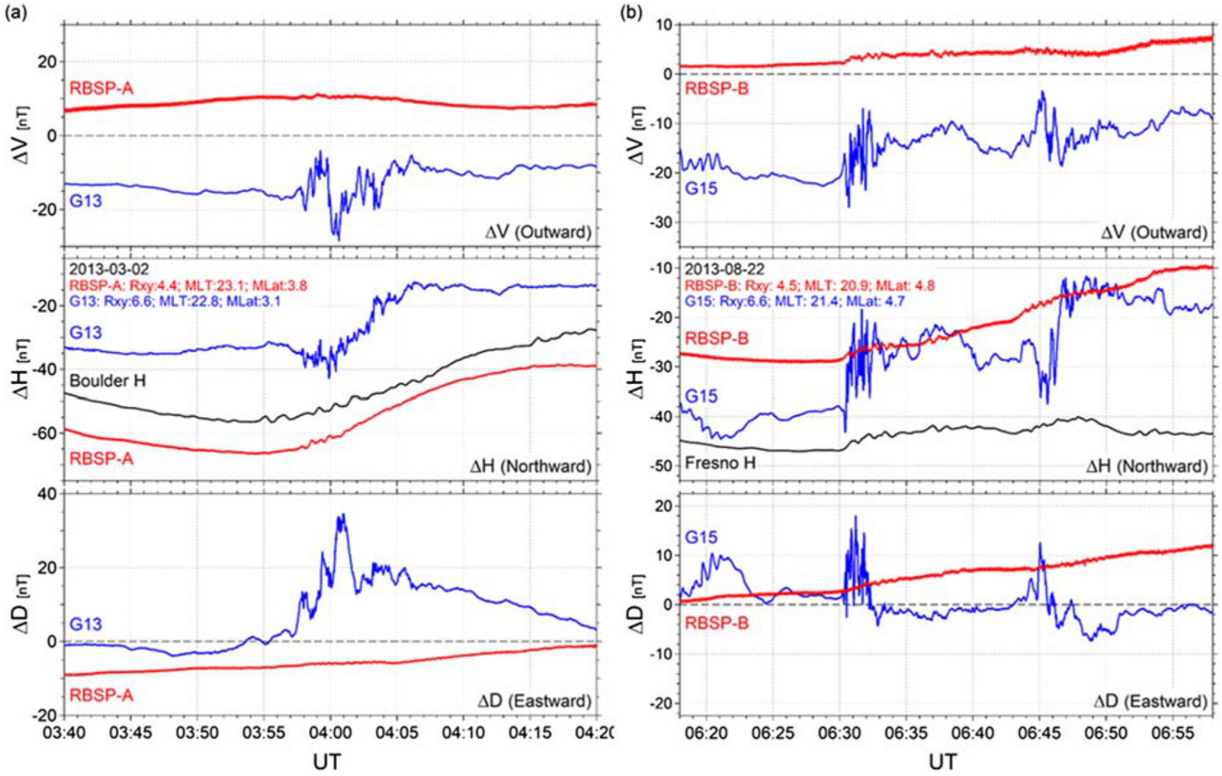

Figure 10. ΔV (top), ΔH (middle), and ΔD (bottom) magnetic components observed by RBSP (red) and GOES (blue) spacecraft in the (a) 2 March 2013 and (b) 22 August 2013 events. The black line in the ΔH panel shows the midlatitude ground H component at Boulder (BOU; offset by −20,850 nT) and Fresno (FRN; offset by −23,610 nT) for the 2 March 2013 and 22 August 2013 events, respectively.

reconfigurations as identified by geosynchronous dipolarizations and midlatitude positive bays. We also found that (3) in the near-Earth region, sharp dipolarizations off the equator often start before geosynchronous dipolarizations. In the following we discuss how these results can be explained in terms of the double-wedge current system (section 1) and what we still need to understand.

Figure 11a schematically shows the two-wedge current system. This figure is basically the same as Figure 8 of O2018 except that the radial profile of ΔH (magenta) has a positive enhancement on the earthward side of the R2CW (blue), which extends to Earth. Dipolarizations at geosynchronous orbit are sustained, which suggests that the R1CW (red) stays outside of geosynchronous orbit. We assume that the R2CW initially forms outside of geosynchronous orbit and proceeds earthward (Ohtani et al., 1990). At the moment shown in Figure 11a, it is already inside geosynchronous orbit. The R1CW is more intense than the R2CW, and therefore, sufficiently away from this double-wedge current system, the remote effect of the R1CW dominates that of the R2CW. However, the effect of the R2CW dominates in its vicinity.

Figure 11a does not specify the current closure in the magnetosphere partly for keeping the figure simple but partly for avoiding speculations, but we like to make five points. First, the tail current intensity is reduced in total as proposed by the conventional SCW model, which results in the overall relaxation of the tail magnetic configuration. The reduced tail current, at least a part of it, should close with FACs forming the R1CW. Second, at the earthward end, the local westward current intensifies in association with dipolarizations (section 3), and it partially closes with FACs forming the R2CW. Third, although in Figure 11a, the FACs are drawn as line currents for simplicity, in reality they are volume currents extending both radially and azimuthally, and so are their closure currents. Fourth, the closure currents also extend along magnetic flux tubes. Accordingly, the total FAC changes with the field-aligned distance from the equator. Finally, there must be additional current loops (i.e., the type-2 system of Boström (1964)) that close meridionally connecting R1CW and R2CW. In this discussion we disregard those meridional current loops since the associated magnetic disturbance is mostly azimuthal, whereas we are concerned with the variations of the H

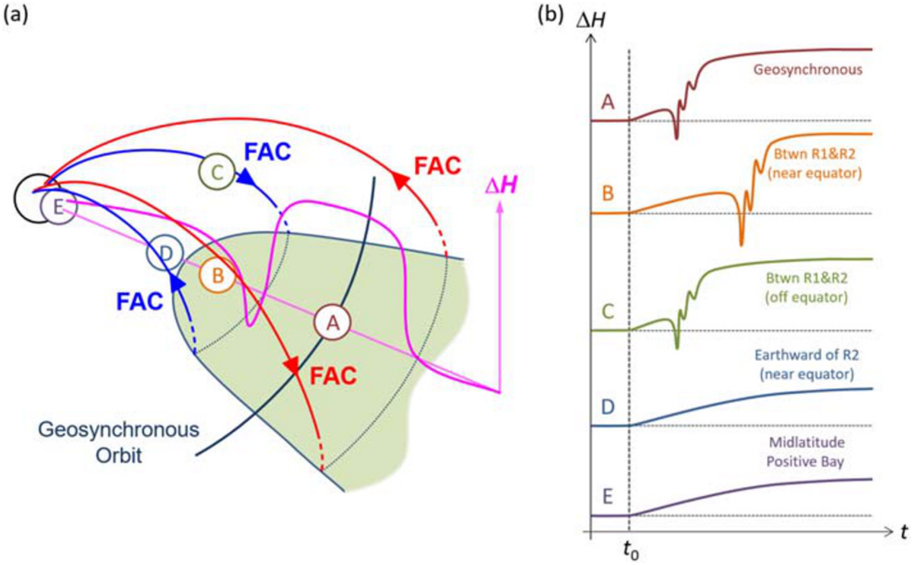

Figure 11. Schematic illustrations of (a) the substorm current system with the R1-sense and R2-sense current wedges, R1CW(red) and R2CW(blue), along with the radial profile of ΔH (magenta), and (b) dipolarization signatures (i.e., ΔH against time, t; t_0: substorm onset) at five different locations A–E shown in Figure 11a.

component. For a more comprehensive set of current loops, see, for example, Figure 5 of Birn and Hesse (2014).

Figure 11b schematically shows the sequence of ΔH at five different points marked in Figure 11a. These five points stay inside the longitudinal sector of the double-wedge current system since its formation at t_0. At geosynchronous orbit, Point A, ΔH starts to increase gradually at t_0 as far as the remote effect of the R1CW is larger than that of the R2CW. Then, as the R2CW approaches from tailward and passes by Point A, ΔH dips and increases sharply. The initial gradual increase in ΔH may not be observed if Point A is too close to the R2CW. At Point B, closer to Earth, the sequence of ΔH is similar but delays from Point A corresponding to the earthward progression of the R2CW. The magnitude of the ΔH increase may be larger at Point B than at Point A because of a geometrical effect; the longitudinal separation of the FACs is smaller closer to Earth. At Point C, at the same r_{xy} as Point B but off the equator, the ΔH sequence is similar, but its timing is earlier than at Point B (because the R2CW passes by earlier) and possibly even earlier than at Point A. At Points A, B, and C, large fluctuations are superposed on the ΔH increase, which can be attributed to either the temporal change of local currents or the spatial structure of currents passing by the spacecraft.

Point D stays earthward of (the final location of) the R2CW at a sufficient distance so that the remote effect of the R1CW dominates that of the R2CW throughout the event, and accordingly, ΔH monotonically increases. Particles injected from the plasma sheet do not reach Point D, and therefore, the change of the local current, if at all, is minimal. Accordingly, the magnetic field changes smoothly (i.e., positive bay-like); it changes so smoothly that superposed Pi2 pulsations can be visually identified. The amplitude of positive bay-like dipolarizations should be smaller than dipolarizations at Points A, B, and C because at Point D, the magnetic effects of the R1CW and R2CW partially cancel each other (Sergeev et al., 2014). The situation is the same at Point E, at midlatitudes on Earth, where ΔH enhancements are identified as positive bays. Thus, the double-wedge model as shown in Figure 11a morphologically explains how dipolarization signatures differ at different radial distances ranging from Earth to geosynchronous orbit.

The R2CW is obviously the key for this generalized SCW model. Whereas the conventional SCW model explains dipolarizations as a remote effect of the R1CW, the double-wedge model interprets (sharp and structured) dipolarizations as a manifestation of the R2CW passing by the spacecraft. The velocity of its earthward motion is considered to be that of the earthward expansion of the dipolarization region, which is statistically estimated at 50 km/s inside geosynchronous orbit ($r \geq 4\ R_E$) (O2018). This velocity is comparable to the earthward expansion velocity of particle injection (Moore et al., 1981; Reeves et al., 1996), and therefore, it is suggested that the R2CW proceeds earthward along with particle injection. It seems that dipolarization and particle injection are different aspects of the same process, rather than one is the cause of the other.

Two nightside processes have been discussed in terms of the double-wedge current system; see Kepko et al. (2015) and references therein. One such process is the formation of fast flow channels, that is, dipolarization fronts, in the plasma sheet (Liu et al., 2013; Yang et al., 2011). The transient reduction of the northward magnetic component such as observed by RBSP-A in the 31 March 2017 event is very often observed prior to dipolarization fronts in the plasma sheet (Ohtani et al., 2004; Runov et al., 2011) and sharp dipolarizations in the near-Earth region (Ohtani et al., 1992) as well as in the inner magnetosphere (Motoba et al., 2018). It is tempting to consider that the earthward expansion of the dipolarization region is the continuous penetration of dipolarization fronts deep into the inner magnetosphere. However, this idea requires another current system for explaining geosynchronous dipolarizations. For dipolarization fronts in the plasma sheet, it was reported that the R2CW is ahead of the R1CW only by a few tenths of 1 R_E (Liu et al., 2013). Therefore, if dipolarizations in the inner magnetosphere are the direct consequence of the deep penetration of dipolarization fronts, the associated R1CW as well as the R2CW would be located inside geosynchronous orbit. However, geosynchronous dipolarizations are very often sustained, which suggests that the R1CW stays mostly outside of geosynchronous orbit. In fact, the R1CW may be located even farther down the tail; for example, in the 31 March 2017 event the B_Z enhancement was also sustained at the THEMIS probes outside of 11 R_E (Figure 7). Therefore, the deep penetration of dipolarization fronts may explain the R2CW but not the R1CW.

The other process that is considered to create a pair of R1CW and R2CW is the braking of fast plasma flows (e.g., Birn et al., 1999; Yang et al., 2012), which naturally explains why the R1 current wedge stays outside of geosynchronous orbit if fast flows stop outside of geosynchronous orbit. Furthermore, a sustained current system that develops subsequently after the flow stopping likely extends tailward as the magnetic flux piles up. On the other hand, it is not clear if, or how, the created R2CW proceeds earthward. If it proceeds earthward as particles are injected by the enhanced electric field, it would mean that the responsible fast plasma flows actually stop in the inner magnetosphere, rather than outside of geosynchronous orbit, and the current system forms and expands both earthward and tailward as they slow down.

Finally, we should point out that the current system associated with dipolarizations in the inner magnetosphere may not represent the M-I system during the substorm expansion phase. Throughout the substorm expansion phase, the westward traveling surge, an intense auroral form near the duskside poleward boundary of the auroral bulge, is collocated with an intense upward FAC (e.g., Fujii et al., 1994). This upward FAC is considered as a primary part of the R1CW, and the surge area is a persistent and critical sink of substorm energy, which is magnetically traced to far tailward of geosynchronous orbit (Ohtani, 2019). On the other hand, the magnetic footprints of the R2CW must be deep inside the auroral bulge, presumably near the location of the initial brightening, where initially intense aurorae become fragile and dissipate during the expansion phase (e.g., Akasofu, 1964). Therefore, although the process associated with dipolarizations in the inner magnetosphere may be critical for the particle transport to the ring current, its role in the energy transport to the ionosphere may be limited in time at the early stage of the substorm expansion phase.

It remains to be a challenge to identify the process responsible for the earthward expansion of the dipolarization region and understand the associated current closure. Nevertheless, the substorm current model of Figure 11, which generalizes the conventional SCW model, seamlessly explains the variability of dipolarization signatures at different radial distances ranging from the ground to geosynchronous orbit and possibly farther out. We believe that it will provide a new critical insight into the initial development of substorms.

6. Summary

In this study we first examined the 31 March 2017 event with multi-satellite data (section 2) and then statistically examined the timing and characteristics of dipolarizations in the inner magnetosphere referring to sharp geosynchronous dipolarizations (section 3). We confirmed that (1) the region of sharp dipolarizations expands earthward while geosynchronous dipolarizations are sustained. We also found that (2) further close to Earth (<5 R_E), positive bay-like dipolarizations start simultaneously with the onsets of global magnetic reconfigurations, and (3) in the inner magnetosphere, dipolarizations off the magnetic equator often start before geosynchronous dipolarizations. The conventional SCW model has serious difficulties in explaining these results as it suggests that dipolarizations take place simultaneously within the wedge.

However, these results can be explained by the double-wedge current system, which consists of R1CW (outside) and R2CW (inside), if (a) the R1CW is more intense than the R2CW in total current, (b) the R1CW stays primarily outside of geosynchronous orbit, and (c) the R2CW moves earthward. According to this model, the region of sharp and structured dipolarizations is confined between the two current wedges, and it expands earthward as the R2CW moves earthward (Result 1). Sufficiently earthward of the R2CW, the remote effect of the R1CW dominates that of the R2CW, and therefore, the local magnetic signature resembles midlatitude positive bays (Result 2). Since the timing of sharp dipolarizations is determined by the passage of the R2CW, at a given radial distance they take place earlier farther off the magnetic equator, and they can even precede geosynchronous dipolarizations especially if the magnetic configuration is stretched (Result 3). Thus, this double-current wedge model explains the characteristics of dipolarization signatures at various radial distances ranging from Earth to geosynchronous orbit and possibly farther out, and it may be regarded as a generalization of the conventional SCW model.

Data Availability Statement

The GOES magnetometer data are available online (at http://www.ngdc.noaa.gov/stp/satellite/goes/dataaccess.html). Ground magnetometer data from Gillam and three midlatitude stations (Fresno, Boulder, and Fredericksburg) were provided by the CARISMA network (PI: Ian Mann) and INTERMAGNET (contact: Alan Thomson), respectively, through the SuperMAG site (http://supermag.jhuapl.edu/; PI: G. W. Gjerloev).

Acknowledgments
The authors thank the Van Allen Probes team, especially C. A. Kletzing and the EMFISIS team, for making the RBSP magnetometer data available through NASA/GSFC Space Physics Data Facility Coordinated Data Analysis Web (https://cdaweb.gsfc.nasa.gov). We are also grateful to V. Angelopoulos and the entire THEMIS team for the THEMIS data, which were provided through the THEMIS Mission website (http://themis.ssl.berkeley.edu). Work at JHU/APL was supported by National Aeronautics and Space Administration (NASA) Grant NNX16AF74G (S. O.), National Science Foundation (NSF) Grant 1603028 (S. O.), JHU/APL Subcontract 937836 to the New Jersey Institute of Technology under NASA Prime Contract NAS5-01072 and NASA Grant 80NSSC20K0699 (T. M.), and NASA Grant NNX15AI95G (K. T.). Work at the University of Colorado is supported by NOAA's Big Earth Data Initiative (BEDI).

References

Akasofu, S.-I. (1964). The development of the auroral substorm. *Planetary and Space Science*, *12*(4), 273–282. https://doi.org/10.1016/0032-0633(64)90151-5

Angelopoulos, V. (2008). The THEMIS mission. *Space Science Reviews*, *141*(1–4), 5–34. https://doi.org/10.1007/s11214-008-9336-1

Auster, H. U., Glassmeier, K. H., Magnes, W., Aydogar, O., Baumjohann, W., Constantinescu, D., et al. (2008). The THEMIS fluxgate magnetometer. *Space Science Reviews*, *141*(1–4), 235–264. https://doi.org/10.1007/s11214-008-9365-9

Birn, J., & Hesse, M. (2014). The substorm current wedge: Further insights from MHD simulations. *Journal of Geophysical Research: Space Physics*, *119*, 3503–3513. https://doi.org/10.1002/2014JA019863

Birn, J., Hesse, M., Haerendel, G., Baumjohann, W., & Shiokawa, K. (1999). Flow braking and the substorm current wedge. *Journal of Geophysical Research*, *104*(A9), 19,895–19,903. https://doi.org/10.1029/1999JA900173

Boström, R. (1964). A model of the auroral electrojets. *Journal of Geophysical Research*, *69*(23), 4983–4999. https://doi.org/10.1029/JZ069i023p04983

Clauer, C. R., & McPherron, R. L. (1974). Mapping the local time-universal time development of magnetospheric substorms using mid-latitude magnetic observations. *Journal of Geophysical Research*, *79*(19), 2811–2820. https://doi.org/10.1029/JA079i019p02811

Fujii, R., Hoffman, R. A., Anderson, P. C., Craven, J. D., Sugiura, M., Frank, L. A., & Maynard, N. C. (1994). Electrodynamic parameters in the nighttime sector during auroral substorms. *Journal of Geophysical Research*, *99*(A4), 6093–6112. https://doi.org/10.1029/93JA02210

Gjerloev, J. W. (2012). The SuperMAG data processing technique. *Journal of Geophysical Research*, *117*, A09213. https://doi.org/10.1029/2012JA017683

Gkioulidou, M., Ohtani, S., Mitchell, D. G., Ukhorskiy, A. Y., Reeves, G. D., Turner, D. L., et al. (2015). Spatial structure and temporal evolution of energetic particle injections in the inner magnetosphere during the 14 July 2013 substorm event. *Journal of Geophysical Research: Space Physics*, *120*, 1924–1938. https://doi.org/10.1002/2014JA020872

Kepko, L., McPherron, R. L., Amm, O., Apatenkov, S., Baumjohann, W., Birn, J., et al. (2015). Substorm current wedge revisited. *Space Science Reviews*, *190*(1–4), 1–46. https://doi.org/10.1007/s11214-014-0124-9

Kletzing, C. A., Kurth, W. S., Acuna, M., MacDowall, R. J., Torbert, R. B., Averkamp, T., et al. (2013). The Electric and Magnetic Field Instrument Suite and Integrated Science (EMFISIS) on RBSP. *Space Science Reviews*, *179*(1–4), 127–181. https://doi.org/10.1007/s11214-013-9993-6

Liou, K., Meng, C.-I., Lui, A. T. Y., Newell, P. T., & Wing, S. (2002). Magnetic dipolarization with substorm expansion onset. *Journal of Geophysical Research*, *107*(A7), 1131. https://doi.org/10.1029/2001JA000179

Liu, J., Angelopoulos, V., Runov, A., & Zhou, X.-Z. (2013). On the current sheets surrounding dipolarizing flux bundles in the magnetotail: The case for wedgelets. *Journal of Geophysical Research: Space Physics*, *118*, 2000–2020. https://doi.org/10.1002/jgra.50092

Mauk, B. H., Fox, N. J., Kanekal, S. G., Kessel, R. L., Sibeck, D. G., & Ukhorskiy, A. (2012). Science objectives and rationale for the Radiation Belt Storm Probes mission. *Space Science Reviews*, *179*(1–4), 3–27. https://doi.org/10.1007/s11214-012-9908-y

McPherron, R. L., Russell, C. T., & Aubry, M. P. (1973). Satellite studies of magnetospheric substorms on August 15, 1968: 9. Phenomenological model for substorms. *Journal of Geophysical Research*, *78*(16), 3131–3149. https://doi.org/10.1029/JA078i016p03131

Moore, T. E., Arnoldy, R. L., Feynman, J., & Hardy, D. A. (1981). Propagating substorm injection fronts. *Journal of Geophysical Research*, *86*(A8), 6713. https://doi.org/10.1029/JA086iA08p06713

Motoba, T., Ohtani, S., Gkioulidou, M., Ukhorskiy, A. Y., Mitchell, D. G., Takahashi, K., et al. (2018). Response of different ion species to local magnetic dipolarization inside geosynchronous orbit. *Journal of Geophysical Research: Space Physics*, *123*, 5420–5434. https://doi.org/10.1029/2018JA025557

Ohtani, S. (1998). Earthward expansion of tail current disruption: Dual-satellite study. *Journal of Geophysical Research*, *103*(A4), 6815–6825. https://doi.org/10.1029/98JA00013

Ohtani, S. (2019). Substorm energy transport from the magnetotail to the nightside ionosphere. *Journal of Geophysical Research: Space Physics*, *124*, 8669–8684. https://doi.org/10.1029/2019JA026964

Ohtani, S., Kokubun, S., Nakamura, R., Elphic, R. C., Russell, C. T., & Baker, D. N. (1990). Field-aligned current signatures in the near-tail region, 2. Coupling between the region 1 and the region 2 systems. *Journal of Geophysical Research*, *95*(A11), 18913. https://doi.org/10.1029/JA095iA11p18913

Ohtani, S., Motoba, T., Gkioulidou, M., Takahashi, K., & Singer, H. J. (2018). Spatial development of the dipolarization region in the inner magnetosphere. *Journal of Geophysical Research: Space Physics*, *123*, 5452–5463. https://doi.org/10.1029/2018JA025443

Ohtani, S., Shay, M. A., & Mukai, T. (2004). Temporal structure of the fast convective flow in the plasma sheet: Comparison between observations and two-fluid simulations. *Journal of Geophysical Research*, *109*, A03210. https://doi.org/10.1029/2003JA010002

Ohtani, S., Takahashi, K., Zanetti, L. J., Potemra, T. A., McEntire, R. W., & Iijima, T. (1992). Initial signatures of magnetic field and energetic particle fluxes at tail reconfiguration: Explosive growth phase. *Journal of Geophysical Research*, *97*(A12), 19311. https://doi.org/10.1029/92JA01832

Reeves, G. D., Friedel, R. W. H., Henderson, M. G., Korth, A., McLachlan, P. S., & Belian, R. D. (1996). Radial propagation of substorm injections, Proceedings of the 3rd International Conference on Substorms, ESA SP-389. (pp. 579–584).

Runov, A., Angelopoulos, V., Zhou, X.-Z., Zhang, X.-J., Li, S., Plaschke, F., & Bonnell, J. (2011). A THEMIS multicase study of dipolarization fronts in the magnetotail plasma sheet. *Journal of Geophysical Research*, *116*, A05216. https://doi.org/10.1029/2010JA016316

Russell, C. T., & McPherron, R. L. (1973). The magnetotail and substorms. *Space Science Reviews*, *15*(2–3). https://doi.org/10.1007/BF00169321

Sergeev, V. A., Nikolaev, A. V., Tsyganenko, N. A., Angelopoulos, V., Runov, A. V., Singer, H. J., & Yang, J. (2014). Testing a two-loop pattern of the substorm current wedge (SCW2L). *Journal of Geophysical Research: Space Physics*, *119*, 947–963. https://doi.org/10.1002/2013JA019629

Tsyganenko, N. A. (1989). A magnetospheric magnetic field model with the warped tail current sheet. *Planetary and Space Science*, *37*(1), 5–20. https://doi.org/10.1016/0032-0633(89)90066-4

Wolf, R. A., Wan, Y., Xing, X., Zhang, J.-C., & Sazykin, S. (2009). Entropy and plasma sheet transport. *Journal of Geophysical Research*, *114*, A00D05. https://doi.org/10.1029/2009JA014044

Yang, J., Toffoletto, F. R., Wolf, R. A., & Sazykin, S. (2011). RCM-E simulation of ion acceleration during an idealized plasma sheet bubble injection. *Journal of Geophysical Research*, *116*, A05207. https://doi.org/10.1029/2010JA016346

Yang, J., Toffoletto, F. R., Wolf, R. A., Sazykin, S., Ontiveros, P. A., & Weygand, J. M. (2012). Large-scale current systems and ground magnetic disturbance during deep substorm injections. *Journal of Geophysical Research*, *117*, A04223. https://doi.org/10.1029/2011JA017415